
Chapter 5: Observations: Oceanic Climate Change and Sea Level

Coordinating Lead Authors: Nathaniel Bindoff, Jürgen Willebrand

Lead Authors: Vincenzo Artale, Anny Cazenave, Jonathan Gregory, Sergey Gulev, Kimio Hanawa, Corinne Le Quéré, Sydney Levitus, Yukihiro Nojiri, C. Shum, Lynne Talley, Alakkat Unnikrishnan

Contributing Authors: J. Antonov, N. Bates, T. Boyer, D. Chambers, J. Church, S. Emerson, R. Feely, H. Garcia, N. Gruber, S. Josey, T. Joyce, K. Kim, B. King, A. Körtzinger, K. Laval, N. Lefevre, R. Marsh, C. Mauritzen, M. McPhaden, C. Millot, C. Milly, R. Molinari, S. Nerem, T. Ono, M. Pahlow, T. Peng, A. Proshutinsky, D. Quadfasel, B. Qiu, S. Rahmstorf, S. Rintoul, M. Rixen, P. Rizzoli, C. Sabine, F. Schott, Y. Song, D. Stammer, T. Suga, C. Sweeney, M. Tamisiea, M. Tsimplis, R. Wanninkhof, J. Willis, P. Woodworth, I. Yashayaev, I. Yasuda

Review Editors: Laurent Labeyrie, David Wratt

Date of Draft: 12 August 2005

Notes: This is the TSU compiled version

Figures

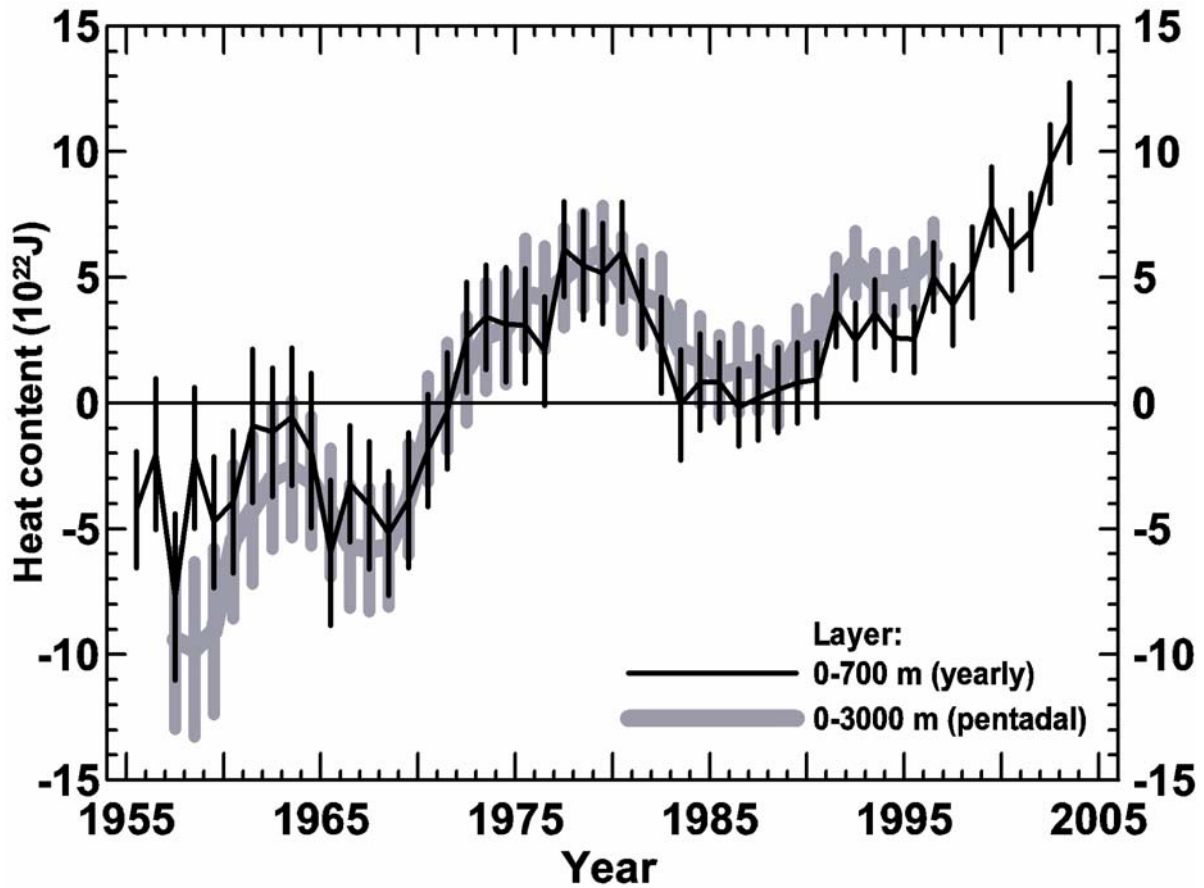
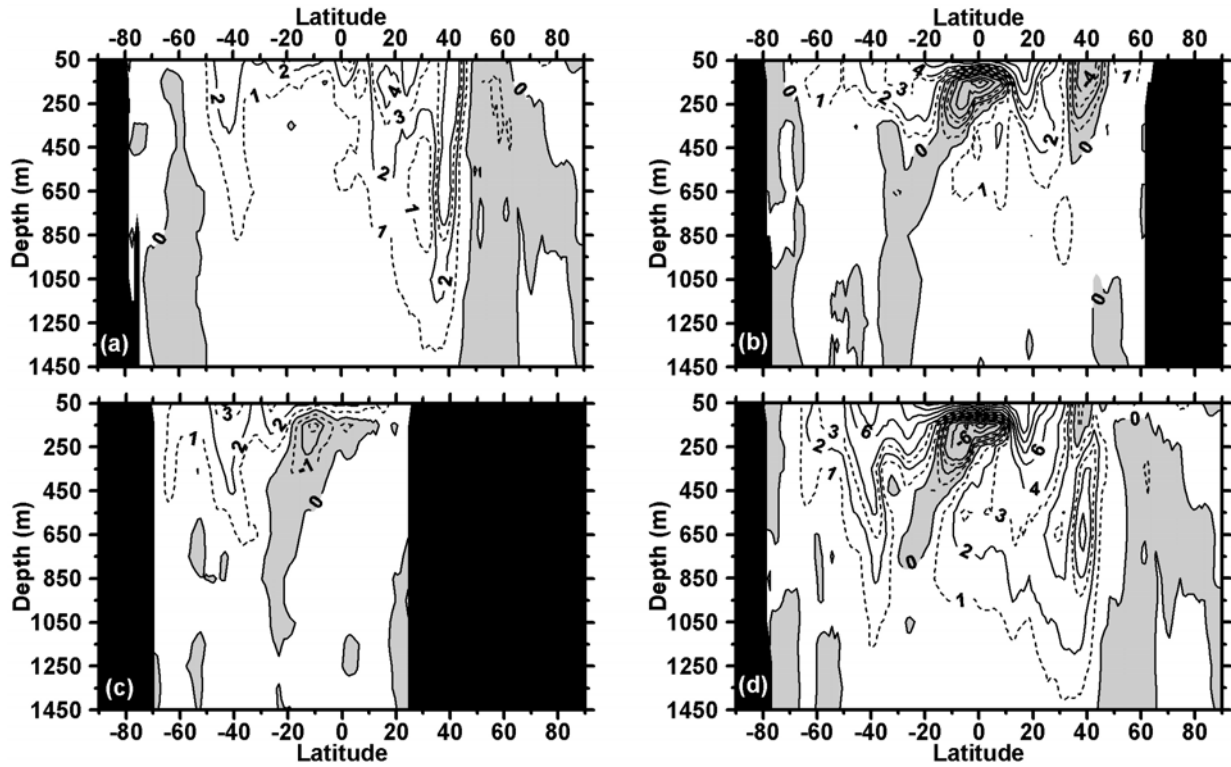


Figure 5.2.1. Time series of yearly ocean heat content (10^{22} J) for the 0–700 m layer and pentadal (5-year running composites for 1955–1959 through 1994–1998) ocean heat content (10^{22} J) for the 0–3000 m layer. Each yearly estimate is plotted at the midpoint of the year, each pentadal estimate is plotted at the midpoint of the 5-year period. Vertical lines through each pentadal (yearly) estimate represent plus and minus one standard error of the pentadal (yearly) estimate about the pentadal (yearly) mean.

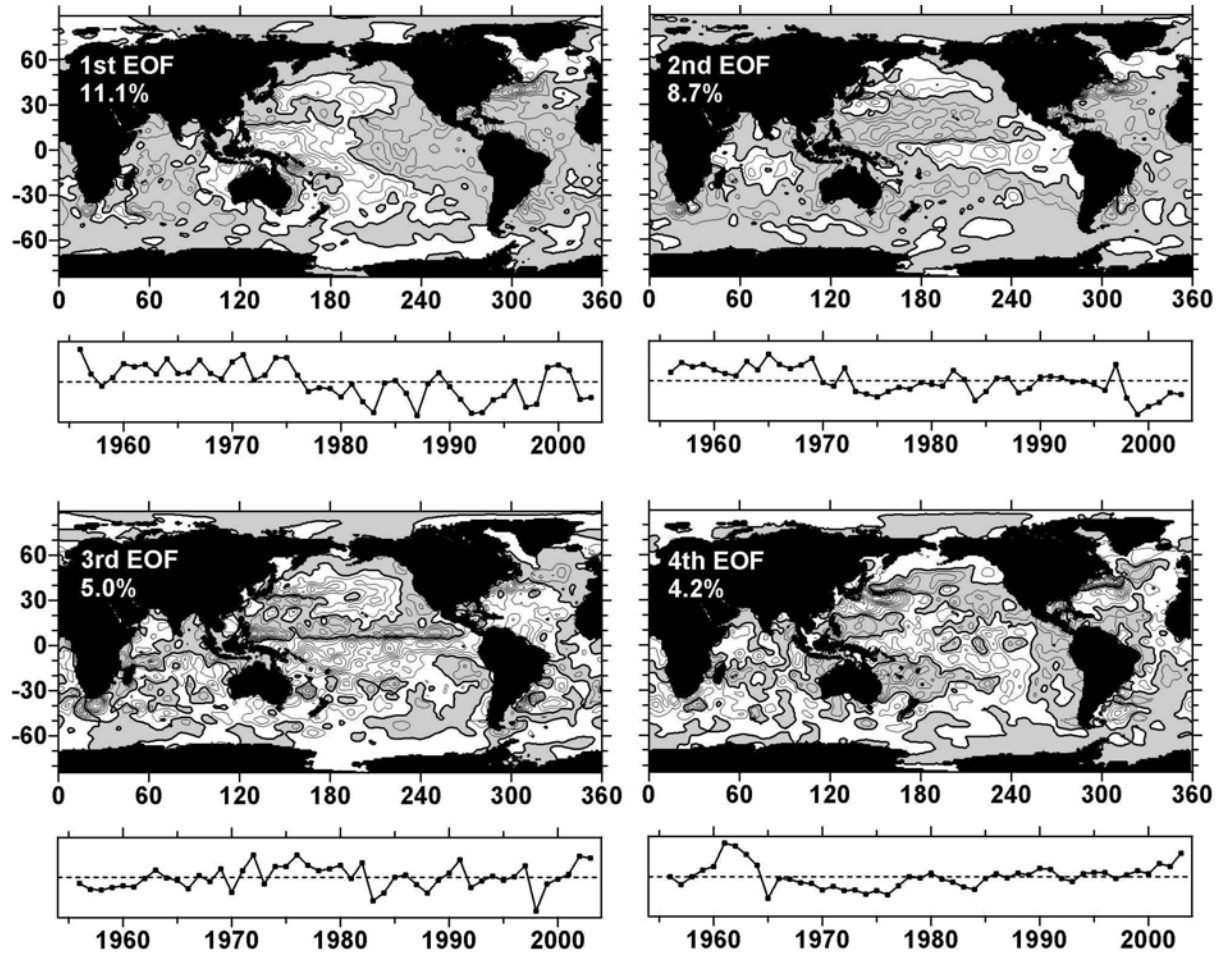
1
2



3
4
5
6
7
8
9
10

Figure 5.2.2. Linear trends (1955–2003) of the zonally integrated heat content by one-degree latitude belts and 100-m thick layers of the a) Atlantic Ocean, b) Pacific Ocean, c) Indian Ocean and d) world ocean. Heat content values are plotted at the midpoint of each 100-m layer. Contour interval is $2 \times 10^{18} \text{ J year}^{-1}$. Negative values are shaded.

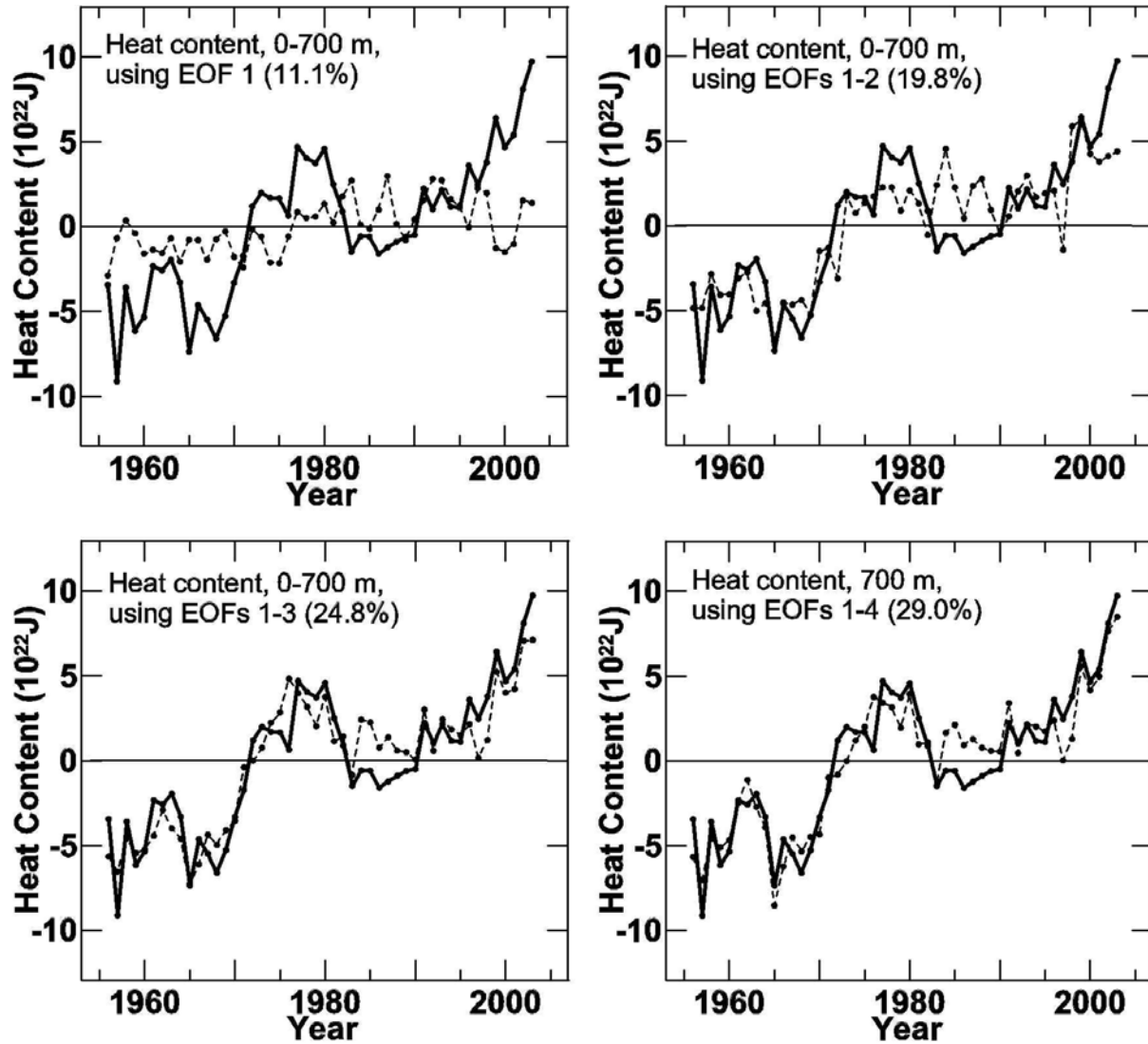
1
2



3
4
5
6
7
8
9
10
11

Figure 5.2.3. EOFs 1 through 4 of 0–700 m ocean heat content and their time variability. The values in each map and time series have been normalized by dividing by the absolute value of the largest value in the map or time series so that all values lie in the range –1 to 1. In the spatial maps heavy black lines represents zero contours and negative values are shaded. The percent variance accounted for by each EOF is given in the top left corner of each spatial map.

1
2



3
4
5
6
7
8
9
10

Figure 5.2.4. Reconstructions of the global, 0–700 m ocean heat content using EOFs 1, 1–2, 1–3, and 1–4. Solid black lines represent the original global heat content integral (Levitus *et al.*, 2005) and dashed black lines represent the reconstructed global heat content integral. The cumulative percent variance accounted for by the EOFs used to reconstruct the heat content integral are given in the top left of each figure.

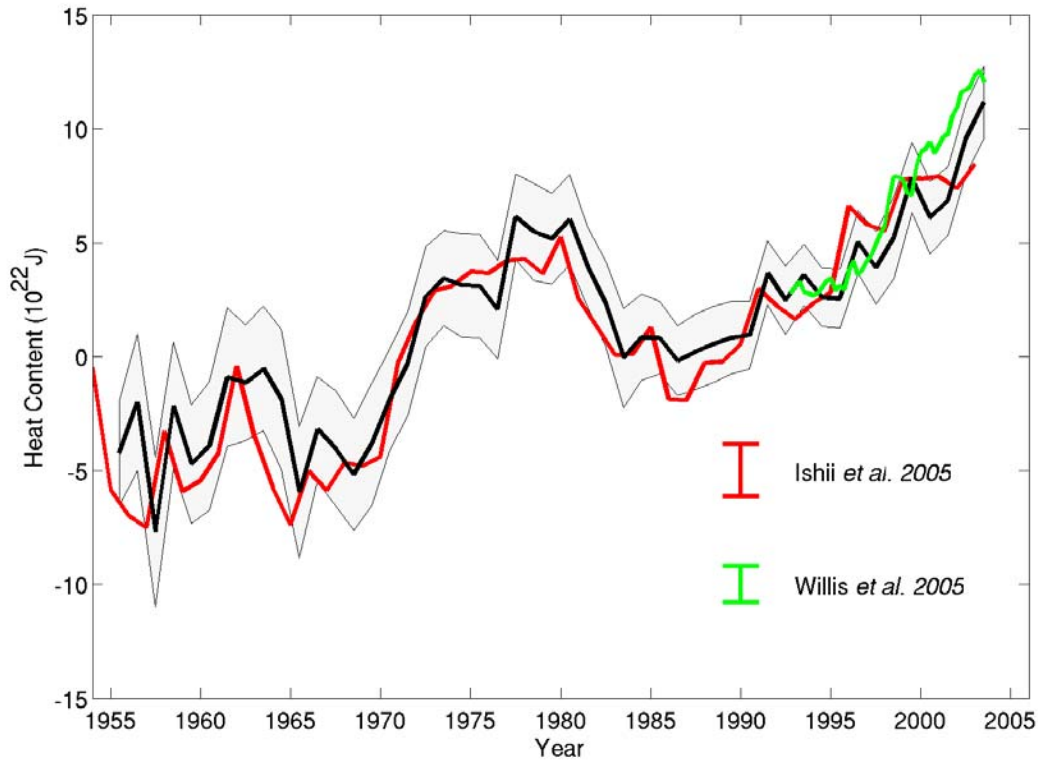
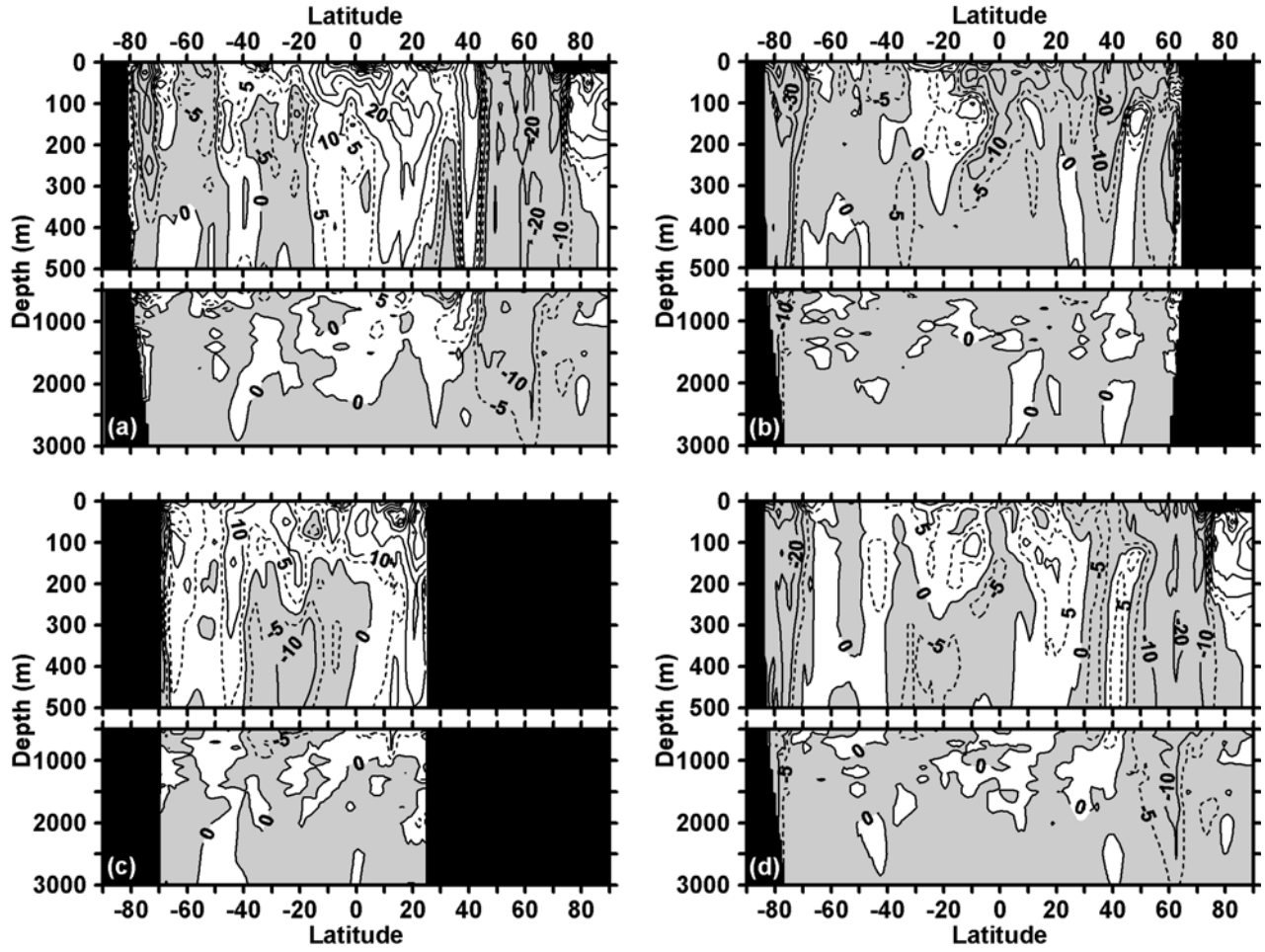
1
23
4
5
6
7
8
9
10
11

Figure 5.2.5. Comparison of the upper ocean heat content for 3 global data sets with error bars. Black, red, and green are the global heat content estimates from Levitus *et al.* (2005a), Ishii *et al.* (2005) and Willis *et al.* (2005). The first two heat content estimates are for 0–700 m layer and the Willis *et al.* (2005) is for 0–750m layer. The standard error for the Levitus *et al.* (2005a) is shown in the shaded area. The standard error is shown separately for the other two data sets.

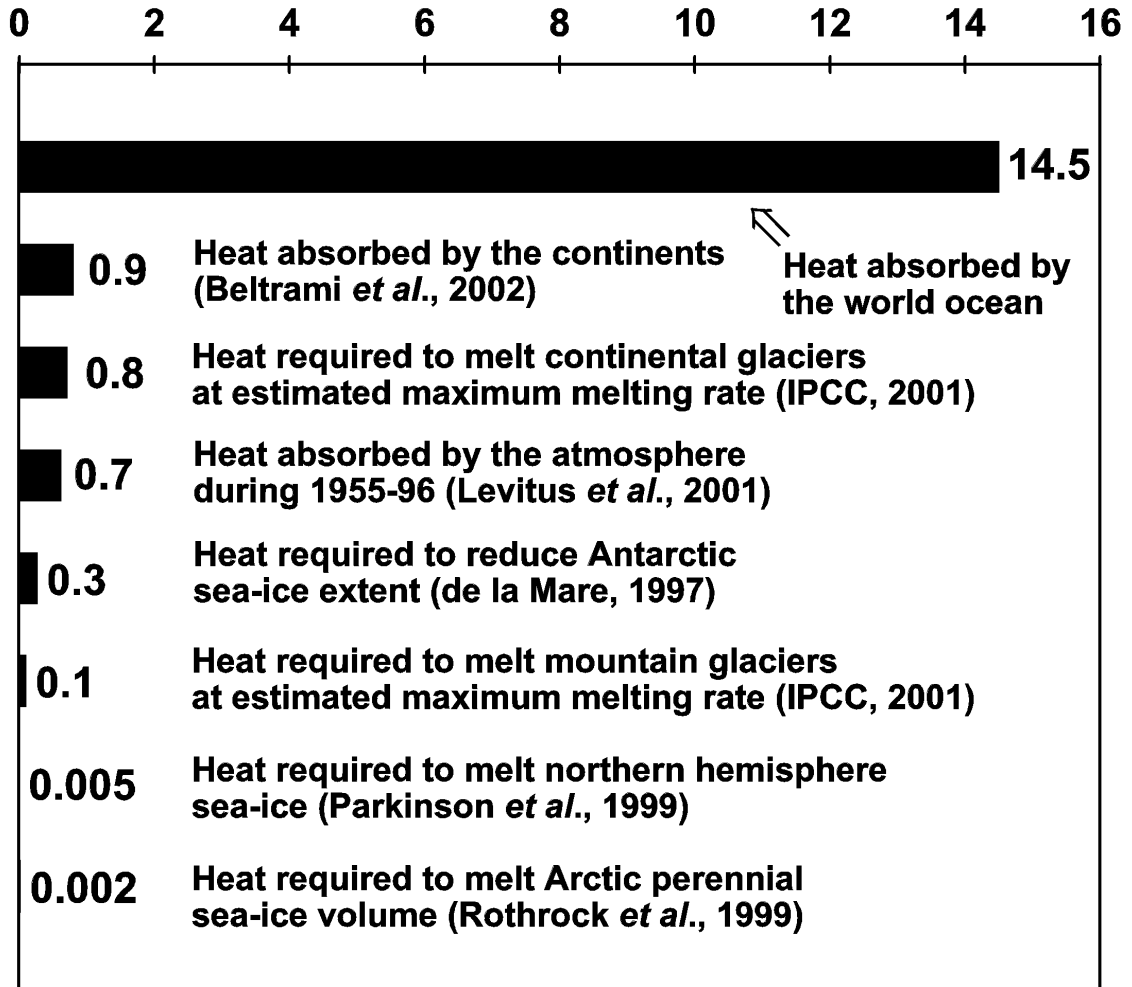
1
2



3
4
5
6
7
8
9
10

Figure 5.2.6. Linear trends (1955–1998) of the zonally averaged salinity of the a) Atlantic Ocean, b) Pacific Ocean, c) Indian Ocean, and d) world ocean by one-degree latitude belts. Contour interval is $10 \times 10^{-4} \text{ year}^{-1}$ (pss). Negative values are shaded.

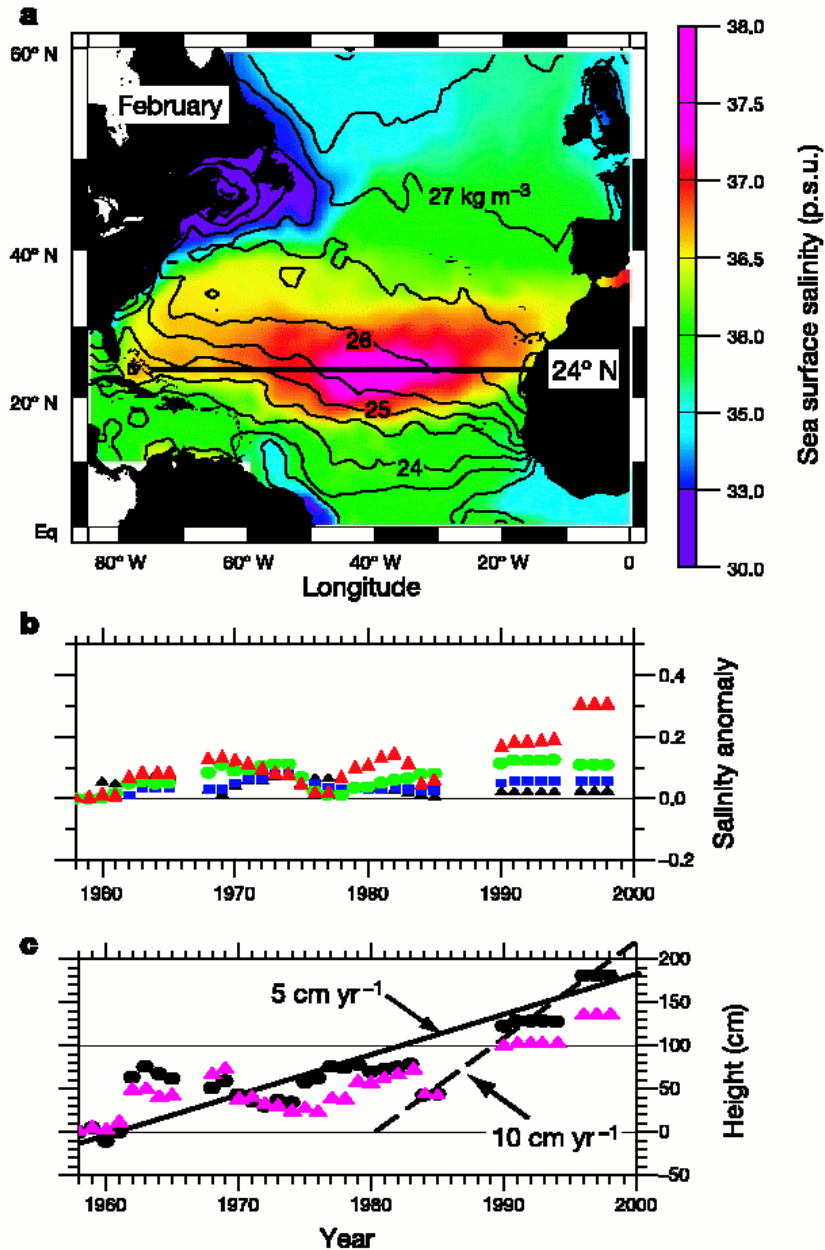
1
2



3
4
5
6
7

Figure 5.2.7. Estimates of earth's heat balance components (10^{22} J) for the 1955–1998 period

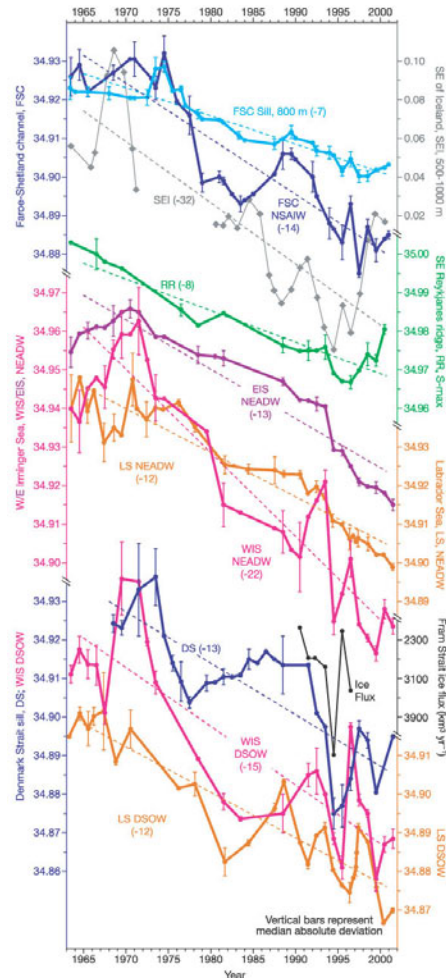
1



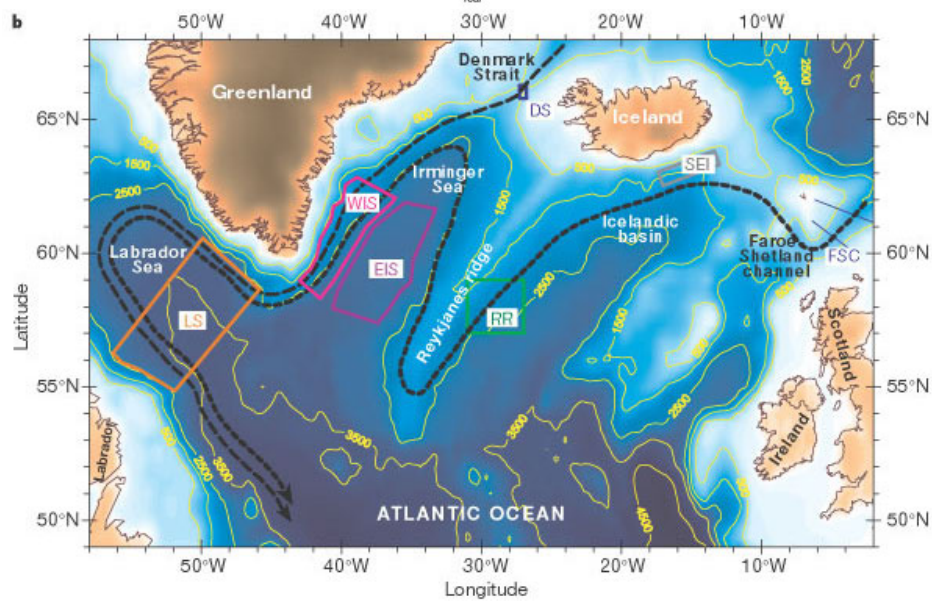
2
3
4
5
6
7
8
9
10
11
12
13
14
15
16
17

Figure 5.3.1. Time series of upper ocean salinity anomalies and estimated E-P anomalies. A, Map of February mean salinity (colour scale) and neutral density (contour interval is 0.5 kg m^{-3}) at the sea surface. The 24N section from which time series were constructed is shown. B, time series of salinity anomaly (relative to the first year in the time series) integrated across 24N for four neutral density layers, $25.5\text{--}26.0 \text{ kg m}^{-3}$ (red triangles), $26.0\text{--}26.5 \text{ kg m}^{-3}$ (green circles), $26.5\text{--}27.0 \text{ kg m}^{-3}$ (blue squares), and $27.0\text{--}27.5 \text{ kg m}^{-3}$ (black triangles). Approximate winter outcrop regions for each layer are shown in A and C. Estimated E-P anomaly for two layers: sea-surface to neutral density 26.5 kg m^{-3} (magenta triangles), and sea-surface to neutral density 27.0 kg m^{-3} (black circles). Each symbol indicates the amount of extra fresh water that would have to be removed per unit area along the section to account for the observed change in salinity of that layer in each year. The slope of the line fitted to the black data points provides an estimate for the rate of change of E-P in cm yr^{-1} . The solid line estimates the E-P anomaly for the entire 42 year record span; the dashed line represents the rate of change estimated for the last 15 years. The y axis is the height of a column of freshwater removed by evaporation to account for the salinity change (Curry *et al.* 2003, Figure 3).

1



2



3

4

5

6

7

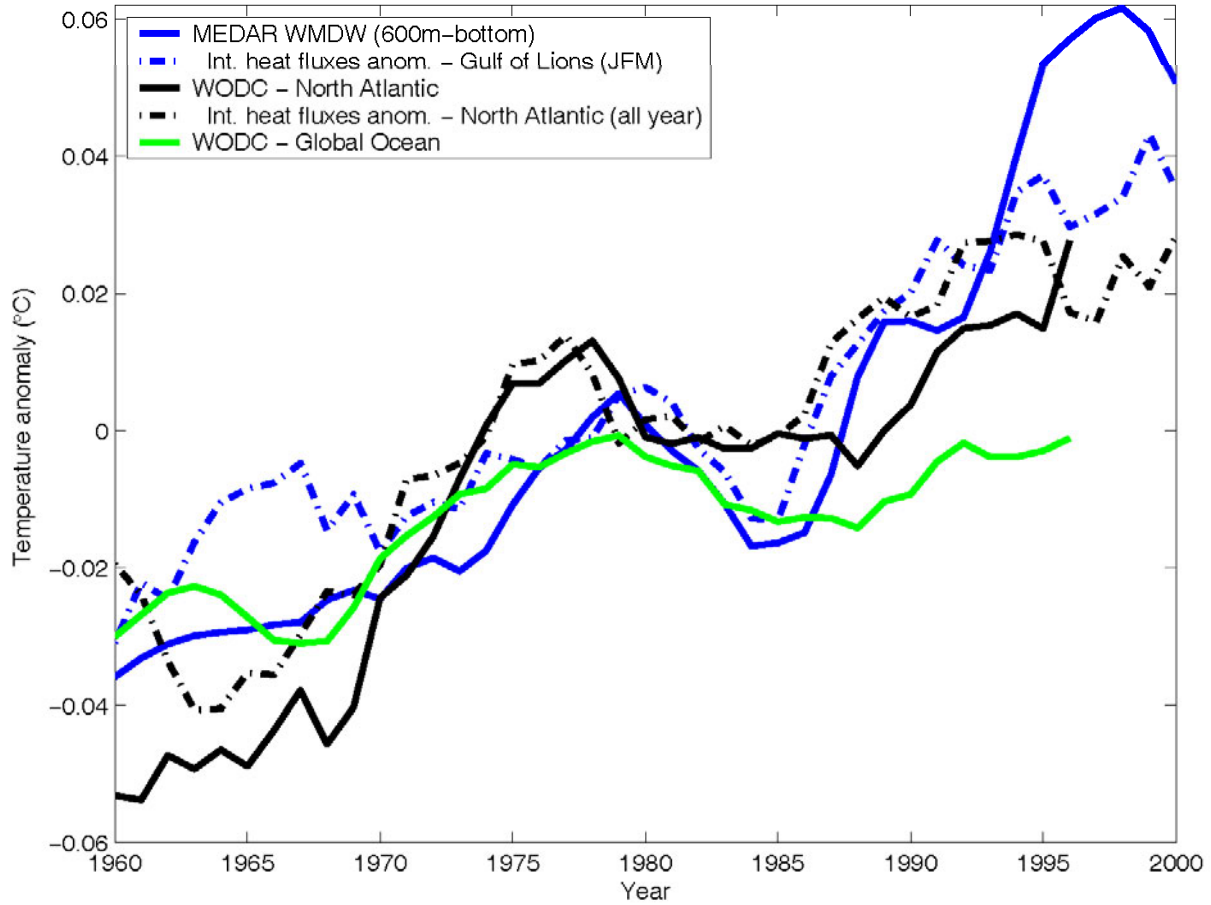
8

9

10

Figure 5.3.2. (a) Salinity time series at various locations in the North Atlantic Polar Gyre. (b) The locations of the time series shown in a). The time series progress clockwise around the gyre starting from the Faroe-Shetland Channel, Reykjanes Ridge, West and East Irmingier Sea, Denmark Strait and Labrador Sea. DSOW is Denmark Overflow Water, NEADW is North East Atlantic Deep Water and NSAIW is reproduced from Dickson *et al.* (2003, their Figure 4).

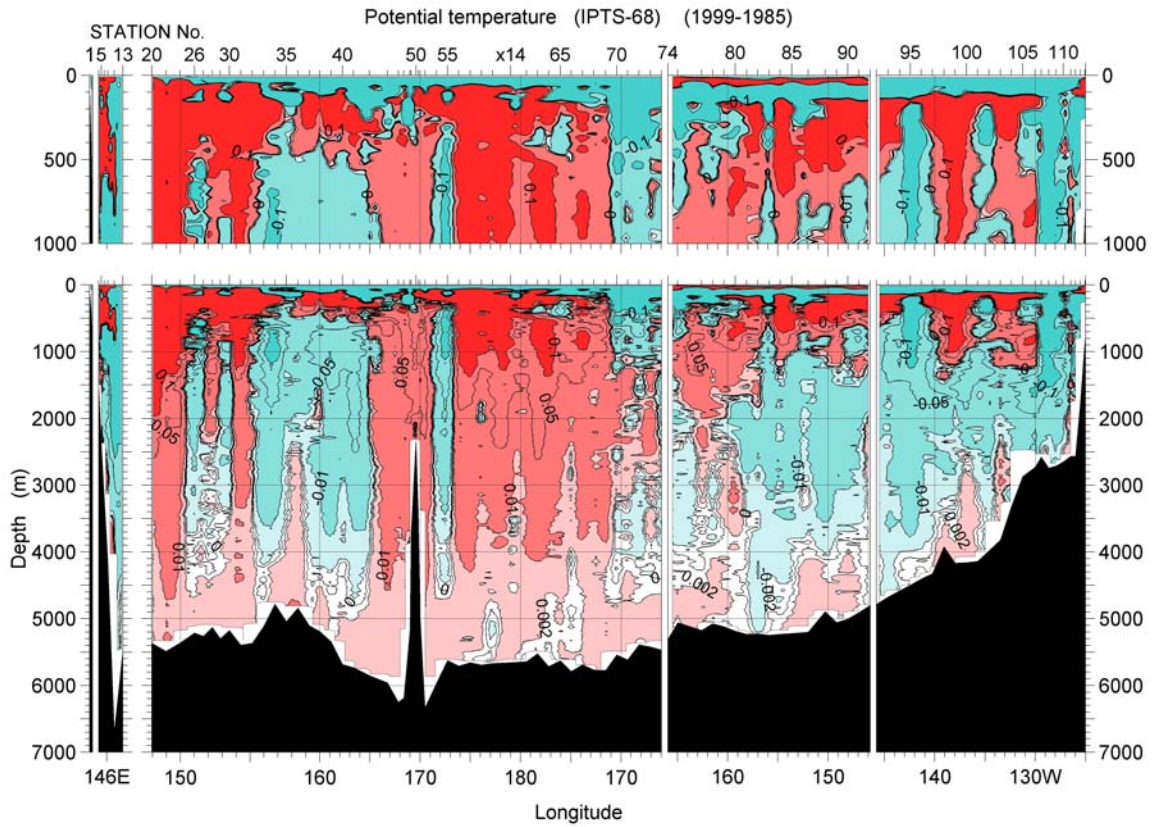
1
2



3
4
5
6
7
8
9
10

Figure 5.3.3. Times series of temperature anomalies (°C), over period 1960–2000, of the MEDAR Western Mediterranean Deep Water (3-year running window, blue), the pentadal North Atlantic (black) and the global ocean (green), and time integrated NCEP-NCAR heat fluxes over the Gulf of Lions (JFM, dashed blue) and the North Atlantic (all-year, dashed black)(Rixen *et al.*, 2005).

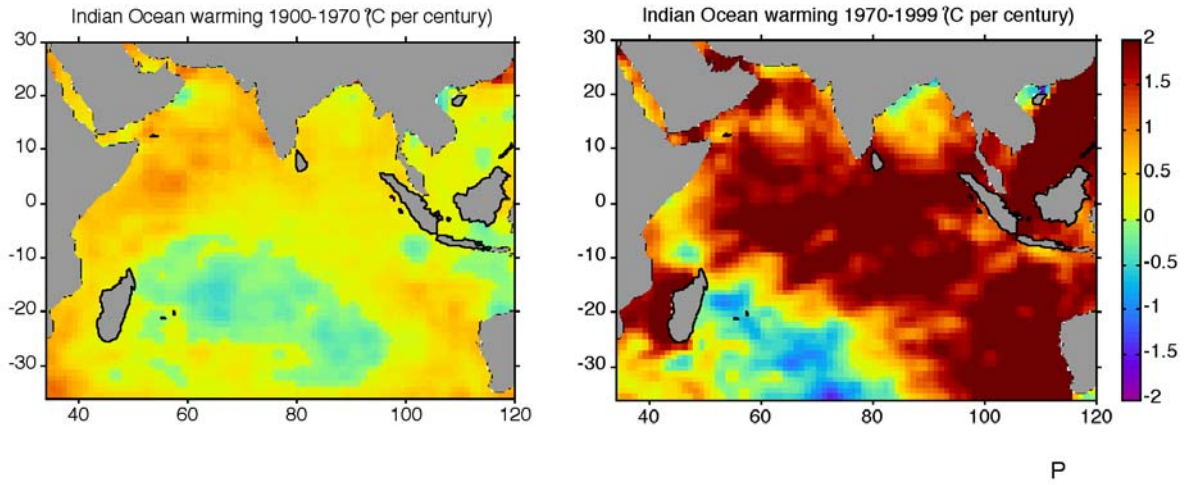
1
2



3
4
5
6
7
8
9

Figure 5.3.4. Changes in temperature below 4000 metres between 1985 and 1999 along a hydrographic section across the North Pacific Ocean at a latitude of 24°N. The measurement accuracy is ~0.001°C (Fukasawa et al, 2004).

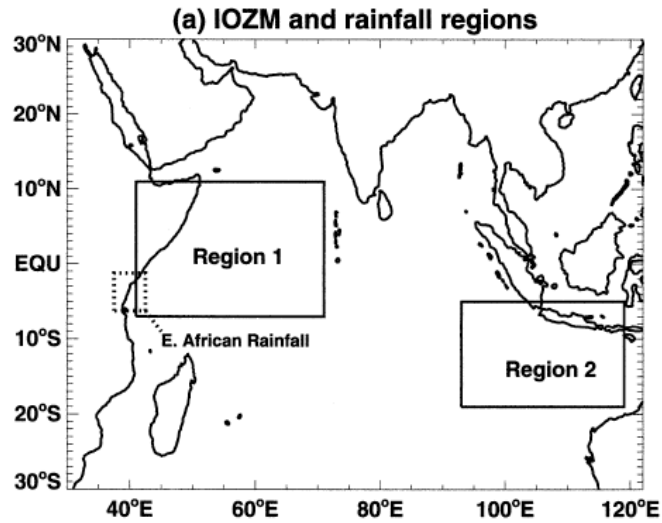
1
2



3
4
5
6
7
8

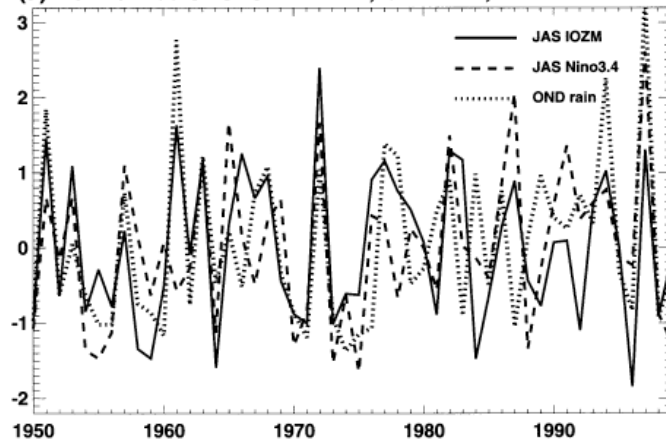
Figure 5.3.5. Linear trend of SST in the Indian Ocean for (a) 1900–1970 and (b) 1970–1999 estimated from the HADISST temperature data (after Rayner *et al.*, 2003).

1
2

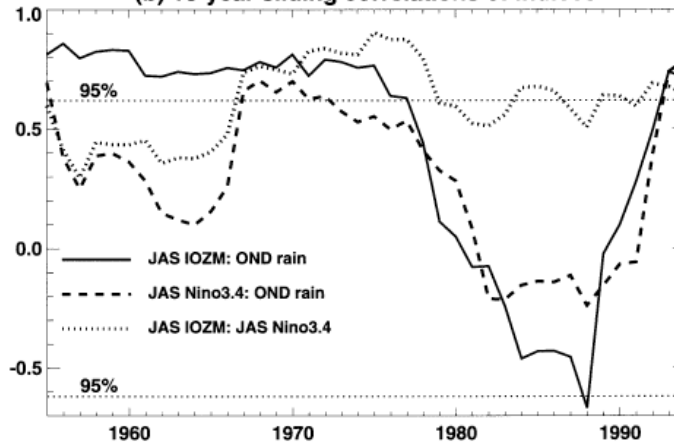


3

(a) Normalized JAS IOZM index, OND rain, and JAS Nino3.4



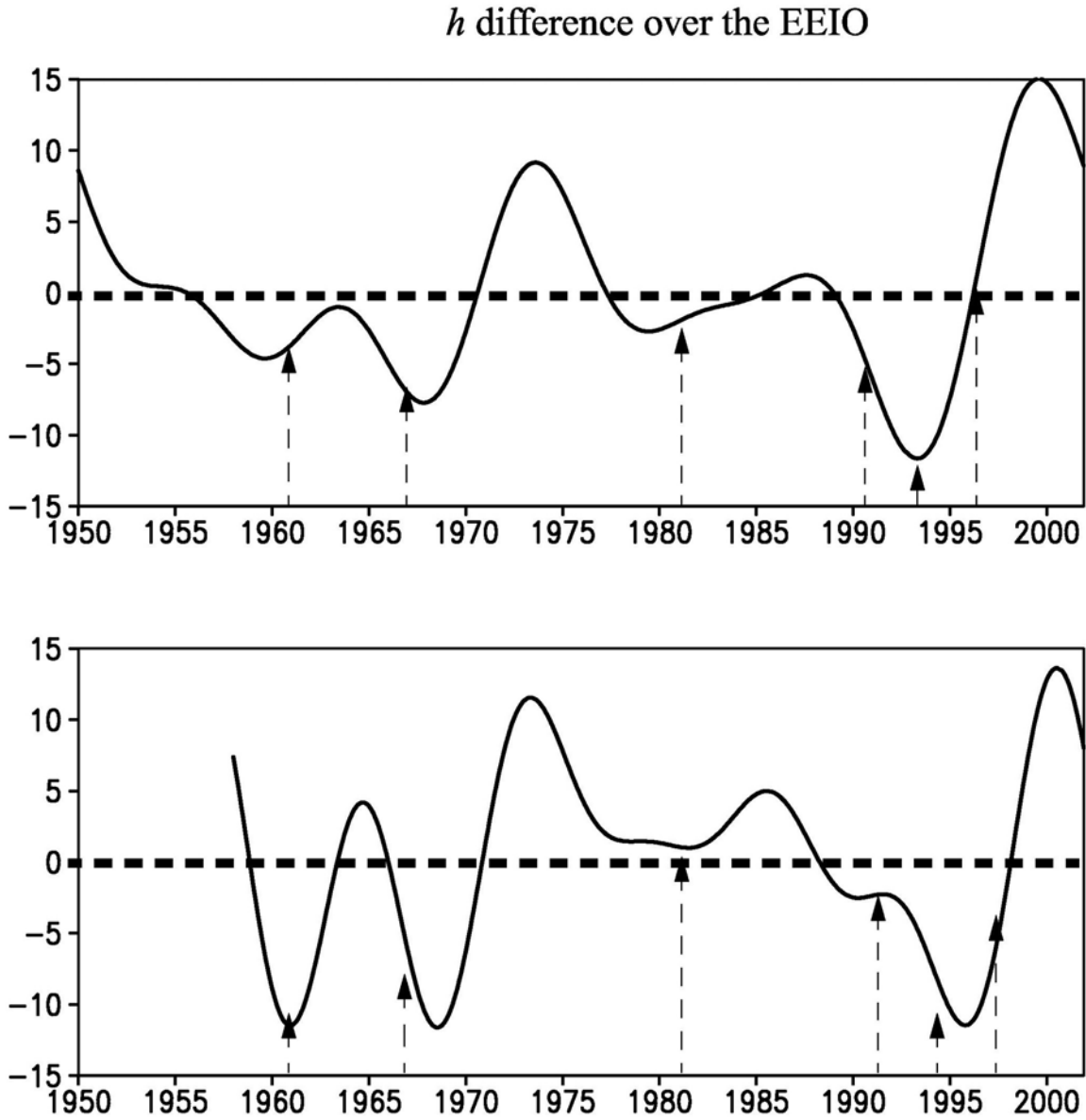
(b) 10-year sliding correlations of indices



4
5
6
7
8
9
10
11

Figure 5.3.6. (a) Location map for East African rainfall and SSTs from the eastern and western basin used for defining Indian Ocean Zonal Mode (IOZM) Index. (b) Time series of normalized IOZM Index (for JAS), African rainfall (for OND) and Nino 3.4 SST (for JAS). (c) Sliding correlations with a 10 yr window between pairs of the 3 curves from b). (From Clark *et al.*, 2003)

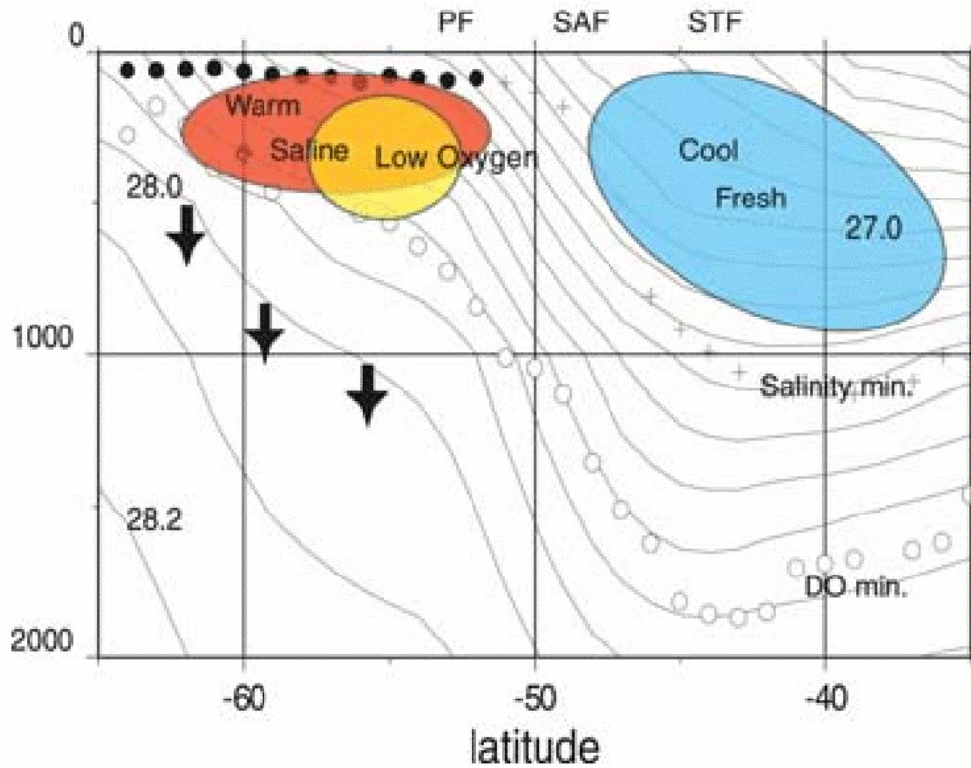
1
2



3
4
5
6
7
8
9

Figure 5.3.7. Variations of Eastern Equatorial Indian Ocean (EEIO) thermocline depth index, derived from ocean model (top) study of Annamalai *et al.* (2004b) and from SODA-POP assimilation product. Dotted vertical lines indicate years of strong IOZM events.

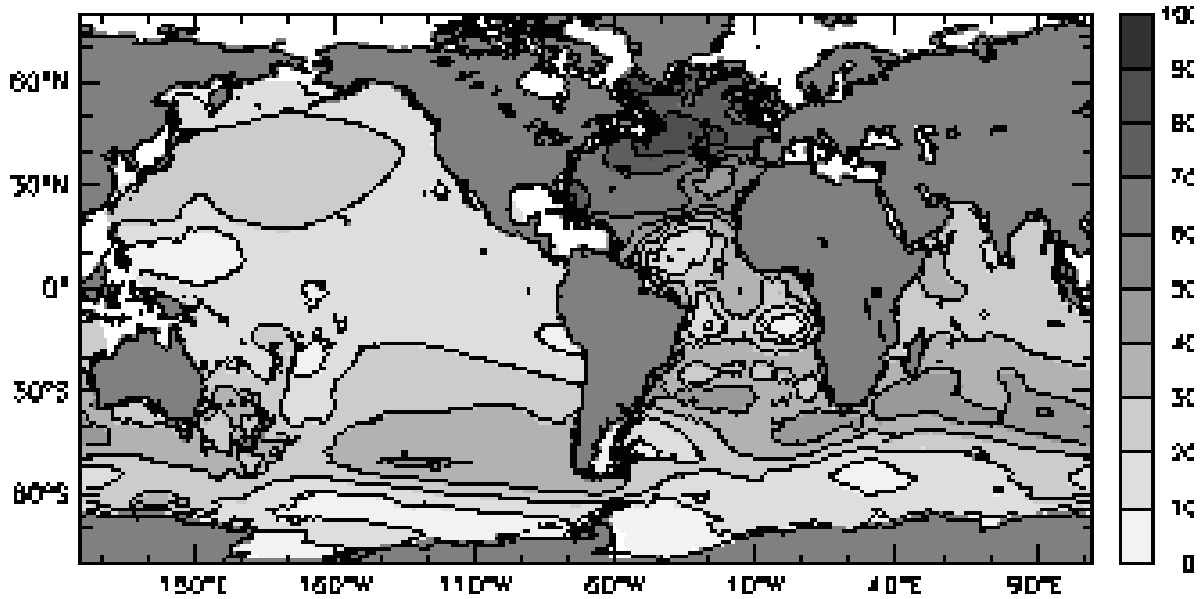
1
2



3
4
5
6
7
8
9
10
11

Figure 5.3.8. A summary of the meridional water mass changes from south of the Antarctic Circumpolar Current from 30°E to 155°E and from 65°S to mid-latitudes (Aoki *et al.* 2005). Cool fresh anomalies are found around the 27.0 kg m⁻³ density surfaces north of the Sub Antarctic Front (SAF). Warm, saline and low oxygen anomalies over the 27.7 to 28.0 kg m⁻³ density surfaces south of the SAF and density surfaces below these densities are now deeper.

1



2

3

4

5

6

7

8

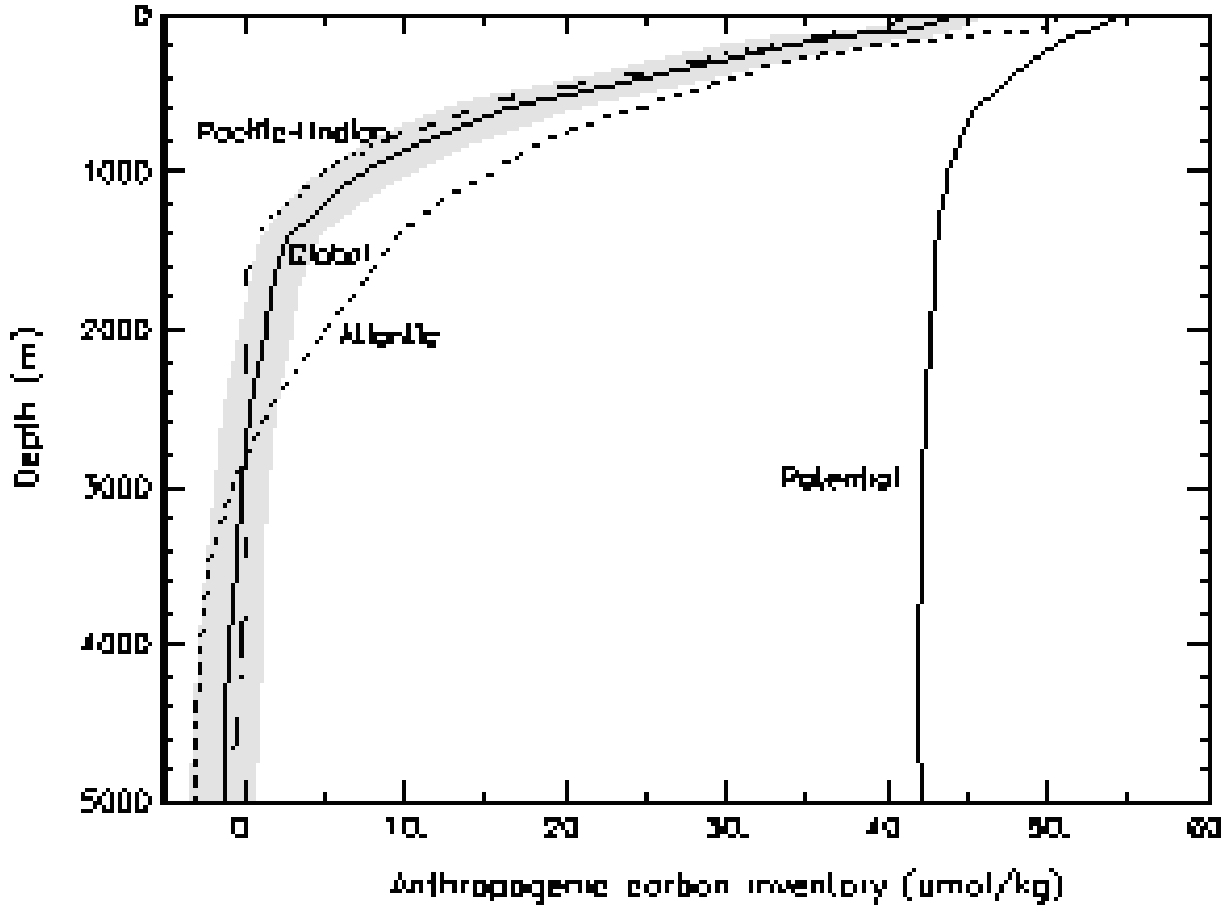
9

10

11

Figure 5.4.1. Inventory of anthropogenic carbon ($\mu\text{mol/kg}$) from Sabine *et al.* (2004). Anthropogenic carbon is estimated indirectly by correcting measured DIC concentrations for the contributions of organic matter decomposition and dissolution of carbonate minerals and taking into account the DIC concentration the water had in the pre-industrial ocean when it was last in contact with the atmosphere. The global inventory of anthropogenic carbon taken up by the ocean is estimated to be $118 \pm 19 \text{ PgC}$ between 1750 and 1994.

1
2



3
4
5
6
7
8
9
10

Figure 5.4.2. Inventory of anthropogenic carbon between 1750 and 1994 averaged over the Atlantic, Pacific and Indian, and Global ocean (umol/kg) (Sabine *et al.*, 2004a). The potential anthropogenic carbon is calculated from carbon chemistry equations, assuming equilibration with an atmospheric CO₂ of 367 ppm (observed in 2000).

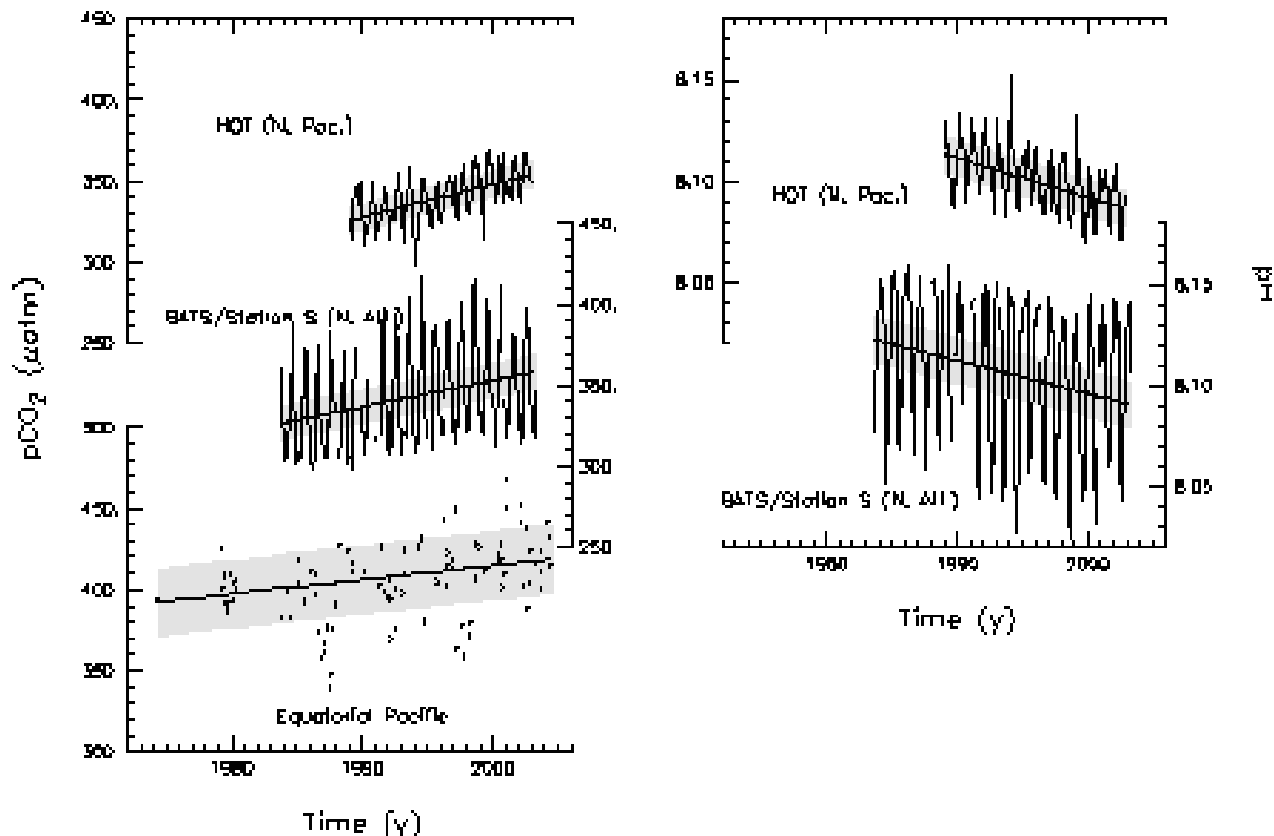
1
23
4
5
6
7
8
9
10
11
12
13
14

Figure 5.4.3. Changes in surface oceanic pCO₂ (left; in µatm) and pH (right) from the HOT (23°N, 158°W) and BATS/Station S (31/32°N, 64°W) time-series stations in the North Pacific (Dore *et al.*, 2003) and North Atlantic (Bates *et al.*, 2002; Gruber and Sarmiento, 2002), and from repeated surveys in the equatorial Pacific (5°S–5°N, 170°W, 120°W; Takahashi *et al.*, 2005). A linear fit to the data is also plotted on each panel. The error bars represent $\pm 1\sigma$ around the deseasonalised values. pCO₂ and pH at time-series stations are computed from local measurements of DIC, alkalinity, temperature and salinity. The pH from HOT is on a total scale at 25°C. Values in the equatorial Pacific are monthly means based on a compilation of measured pCO₂ data.

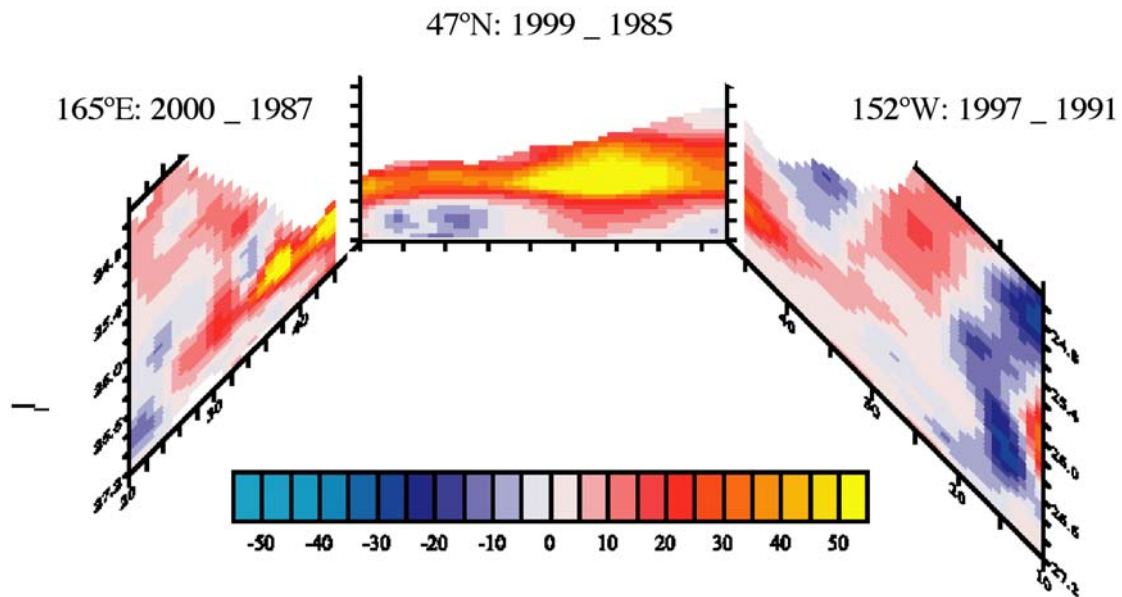
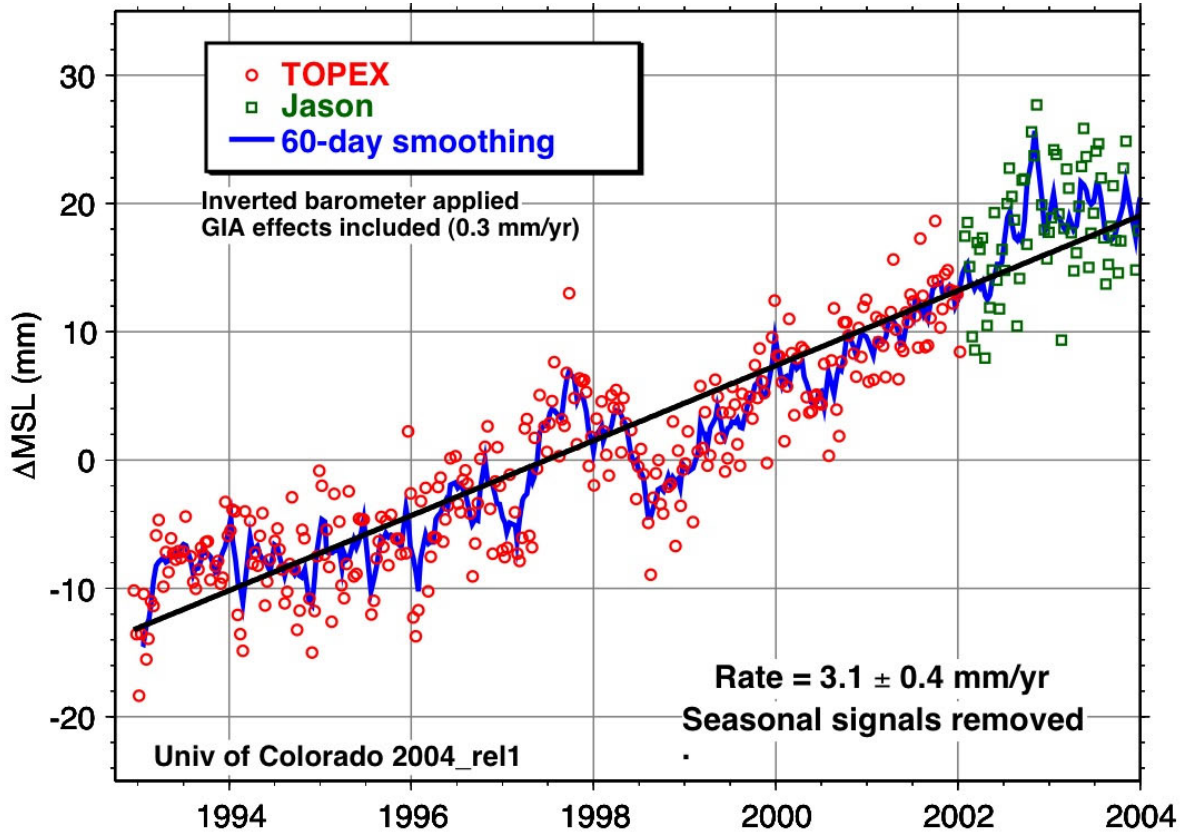
1
23
4
5
6
7
8
9

Figure 5.4.4. Changes in Apparent Oxygen Utilization (AOU: $\mu\text{mol}/\text{kg}$) along three cruise tracks in the North Pacific at 165E, 47N, and 152W. Each section represents the difference between AOU measured once in the 1980s and again in the 1990s, although specific cruise years differ among sections. Sections are plotted on density intervals. Figure from Deutsch *et al.* (2005).

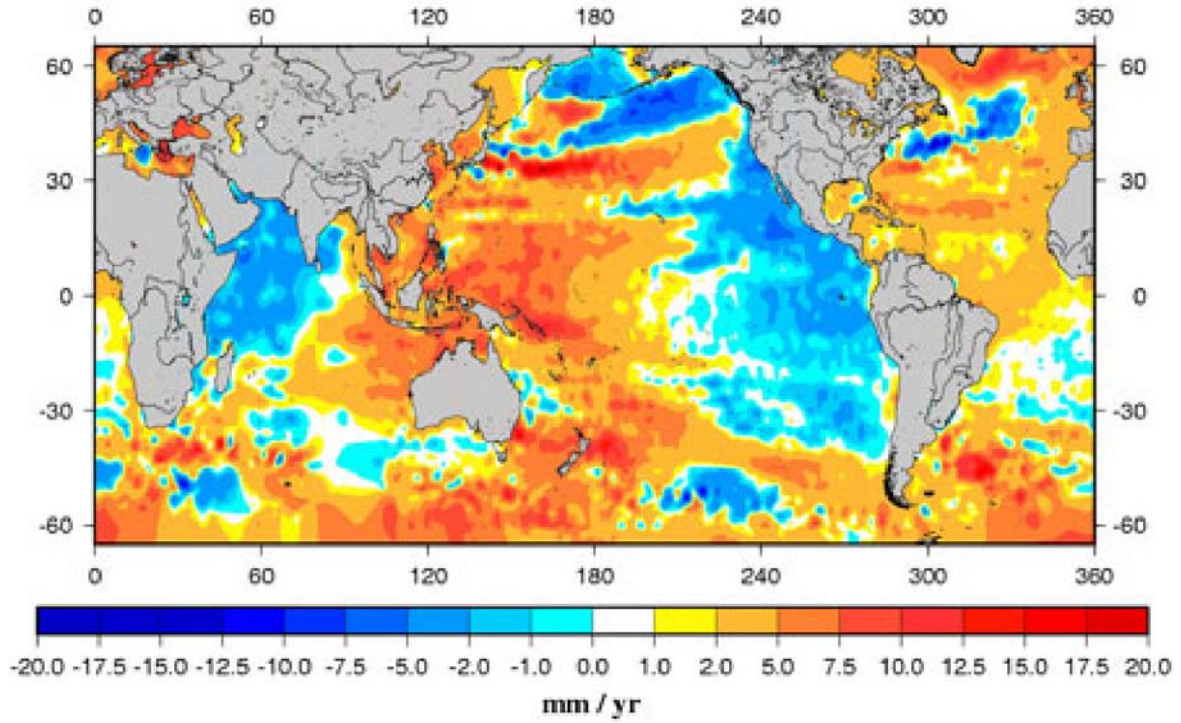
1
2



3
4
5
6
7
8

Figure 5.5.1. Variations in global mean sea level compute from TOPEX and Jason altimeter data (updated from Cazenave and Nerem, 2004; Leuliette *et al.*, 2004).

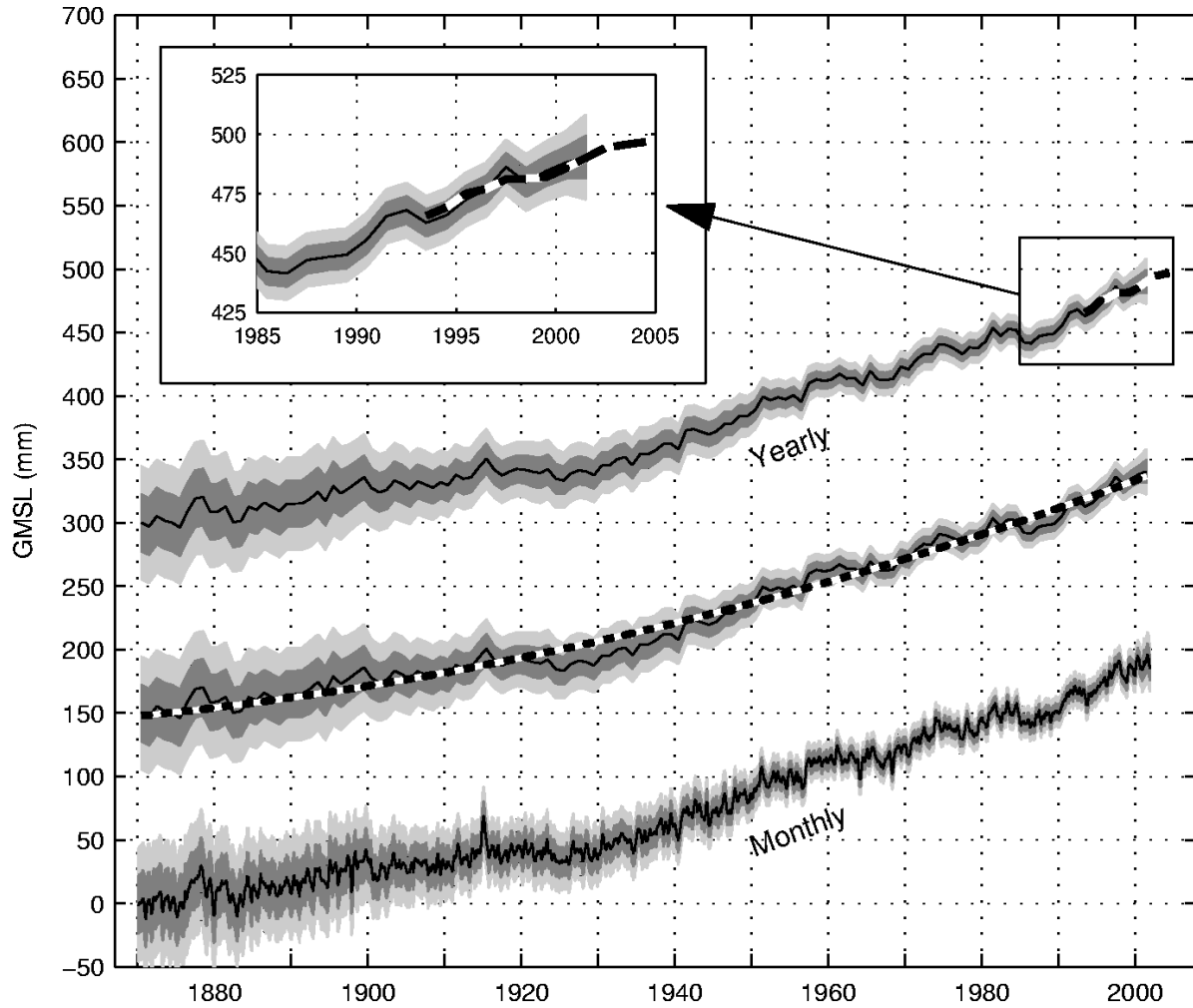
1
2



3
4
5
6
7
8

Figure 5.5.2. Geographic variations in sea level rise over 1993–2005 (updated from Cazenave and Nerem, 2004).

1
2



3
4
5
6
7
8
9
10
11
12

Fig. 5.5.3. Annual averages of the global averaged sea-level between 1870 and 2000 from the reconstructed sea-level fields. The insert shows the comparison between the reconstructed field from tide gauges and the Topex/Poseidon altimeter (dashed line). The three reconstructed curves are the monthly global average, the yearly global average with quadratic fit to the data and the yearly average. The shaded area are 1 (dark) and 2 (light) standard deviation error estimates from the reconstructed fields.

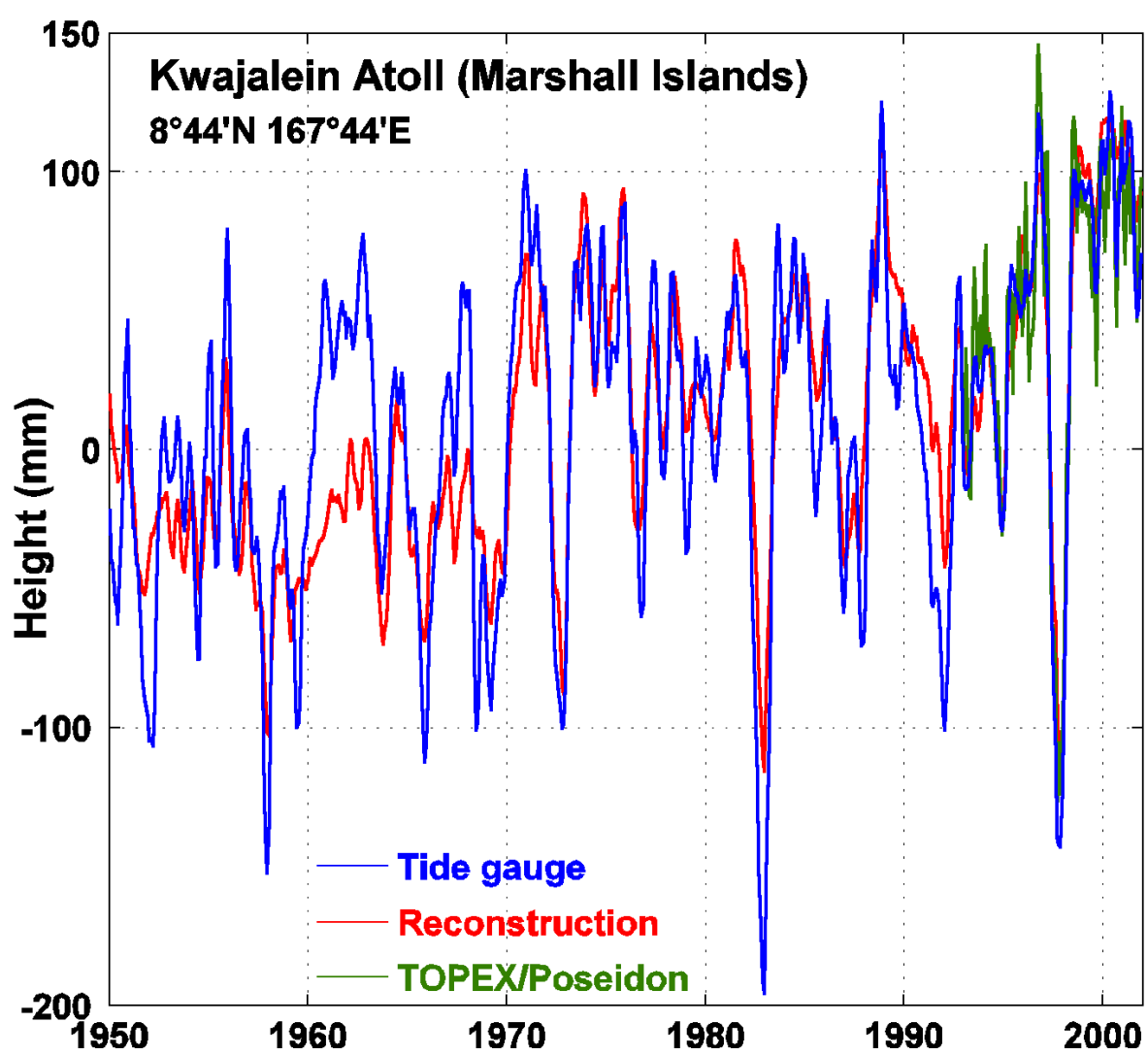
1
23
4
5
6
7
8
9
10
11

Figure 5.5.4. Monthly mean sea-level data between 1950 and 2000 for Kwajalein (8°44'N, 167°44'E). The observed sea level is in blue, the reconstructed sea level in red and the satellite altimetry record in green. All of the time series have had the annual and semi-annual signals removed and the tide gauge data have been smoothed (from Church *et al.*, 2005b).

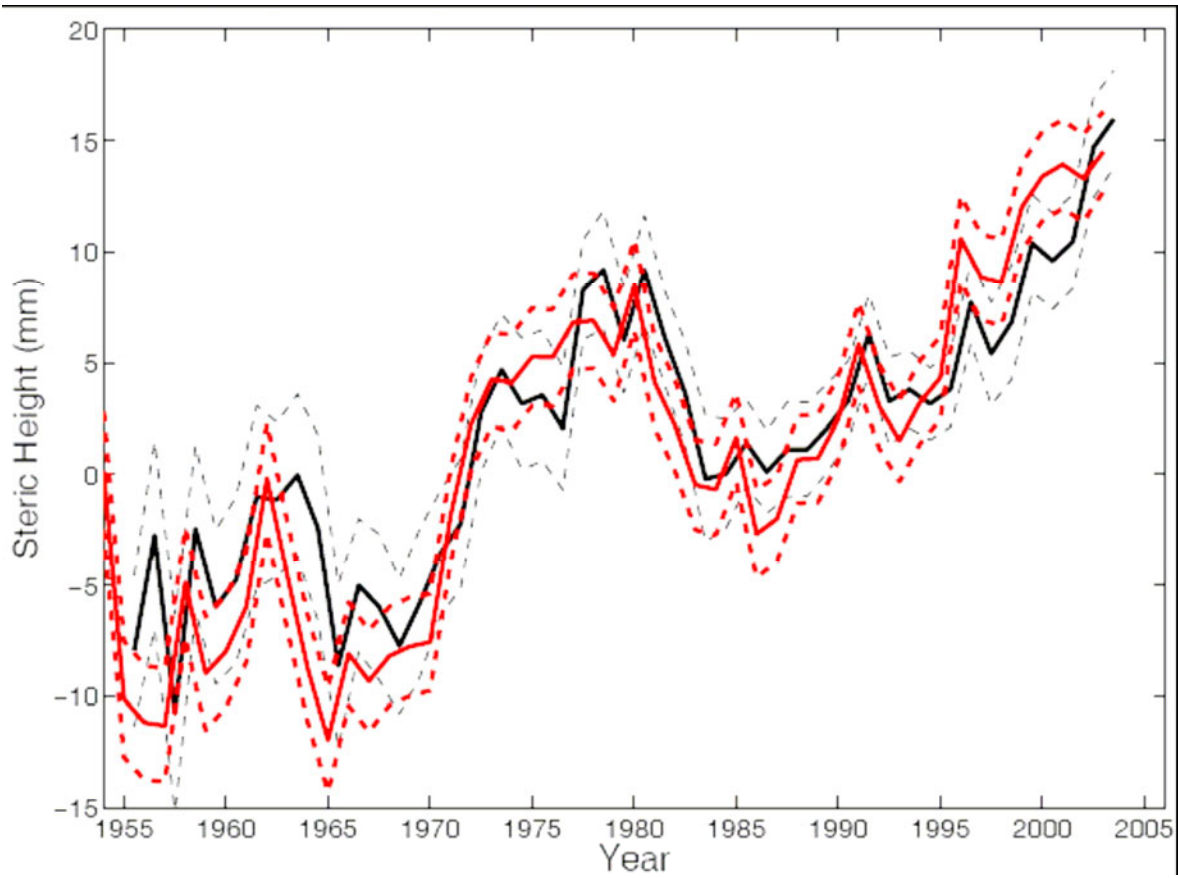
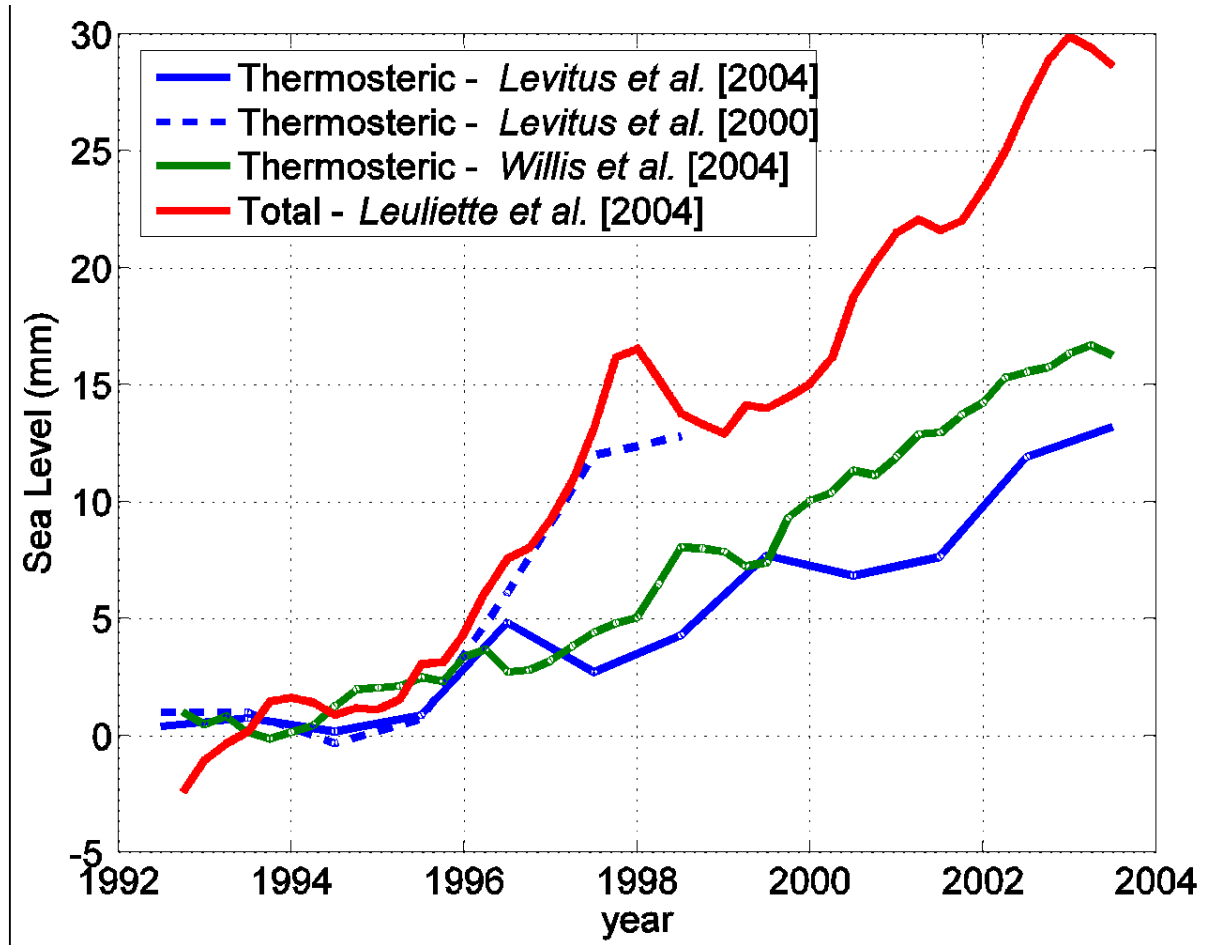
1
23
4
5
6
7
8
9

Figure 5.5.5. Steric sea level curve for 1950–2003, the 0–700 m layer, average over 90N–90S based on the Levitus *et al.* (2005) data (black curve, dashed lines are standard errors) and Ishii *et al.* (2005) data (red curve, also with standard errors).

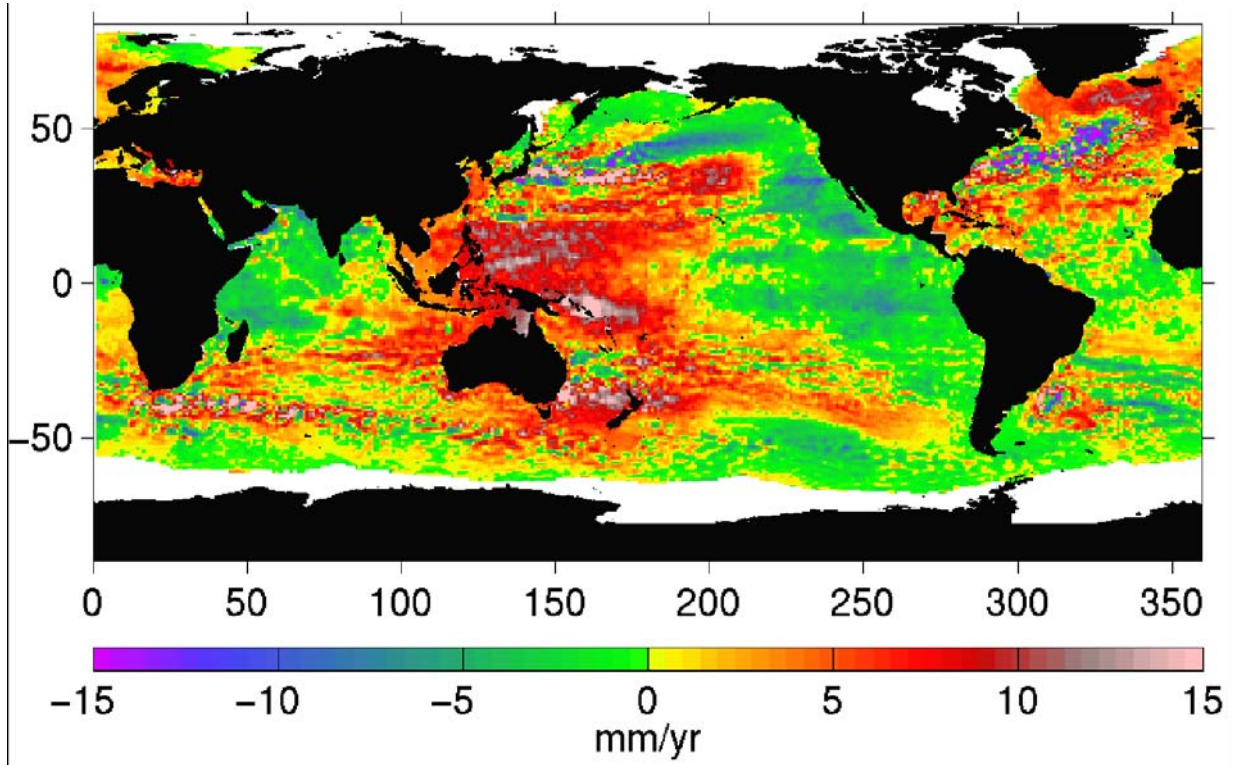
1
2



3
4
5
6
7
8
9
10

Figure 5.5.6. Mean yearly-average thermosteric sea level variation in the 1990s based on analysis by different groups, compared with total sea level variation measured by the Topex/Poseidon altimeter (from Willis *et al.*, 2004).

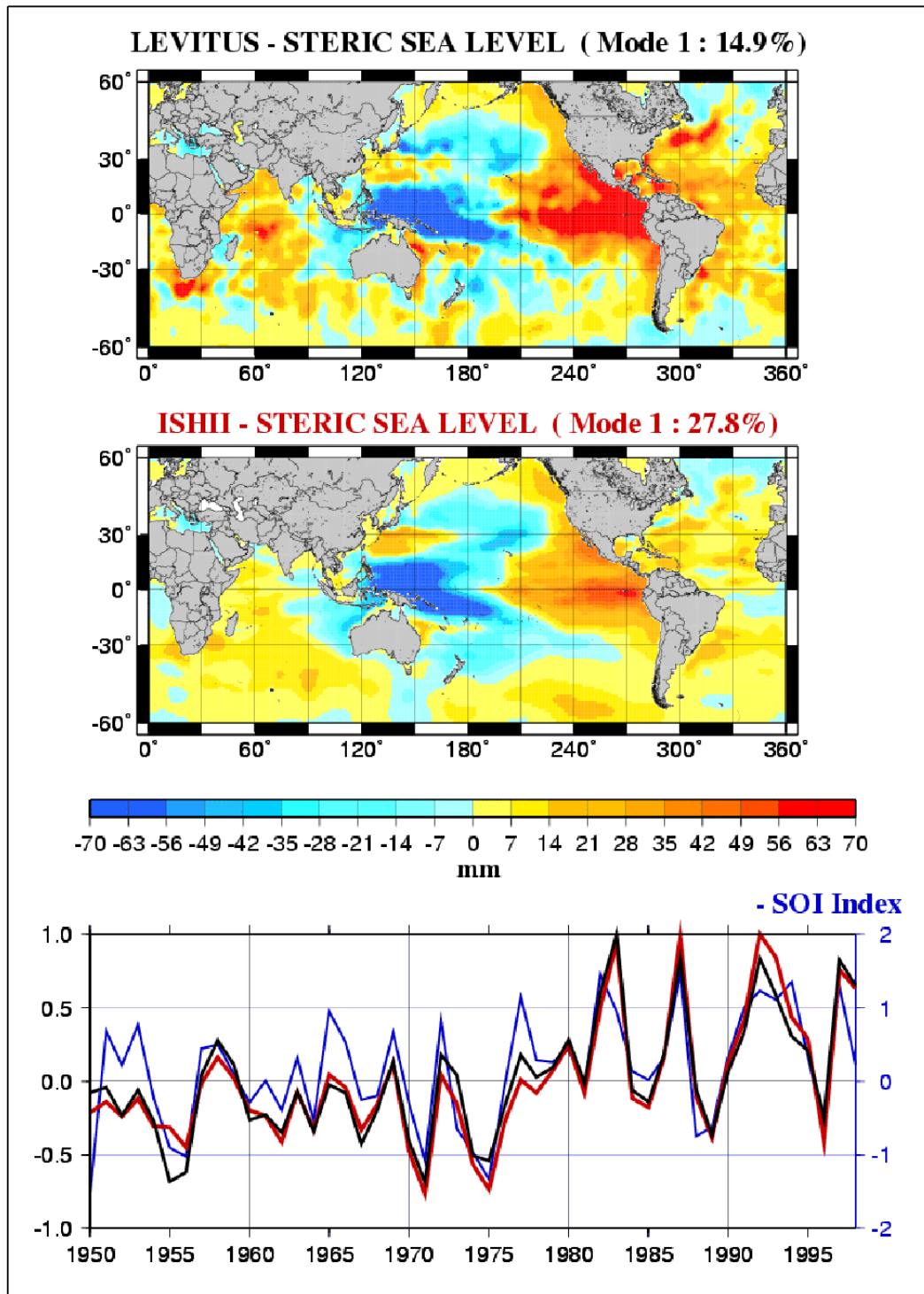
1
2



3
4
5
6
7
8
9

Figure 5.5.8. Geographical distribution of trends in thermosteric sea level from 1993 to 2003 (from Willis *et al.*, 2004)

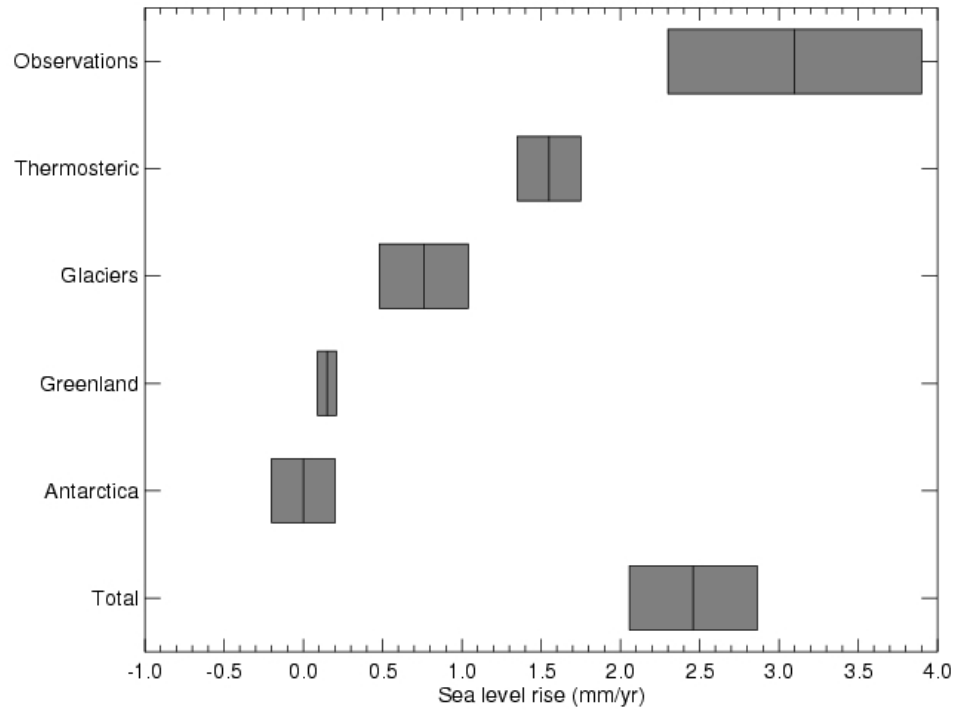
1
2



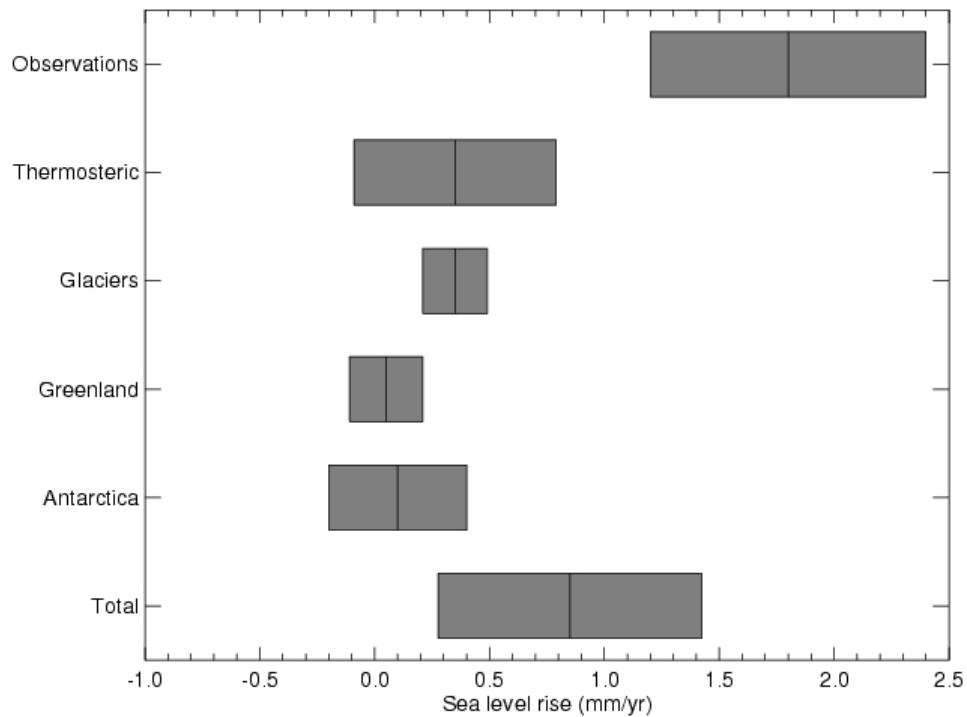
3
4
5
6
7
8
9
10

Fig. 5.5.9. First mode of the EOF decomposition of the gridded steric sea level time series from Levitus *et al.* (2000) and Ishii *et al.* (2003). The bottom panel shows the associated temporal curves (black curve : Levitus; red curve : Ishii). The SOI (southern oscillation index) is superimposed (blue curve) (from Lombard *et al.*, 2005b)

1
2



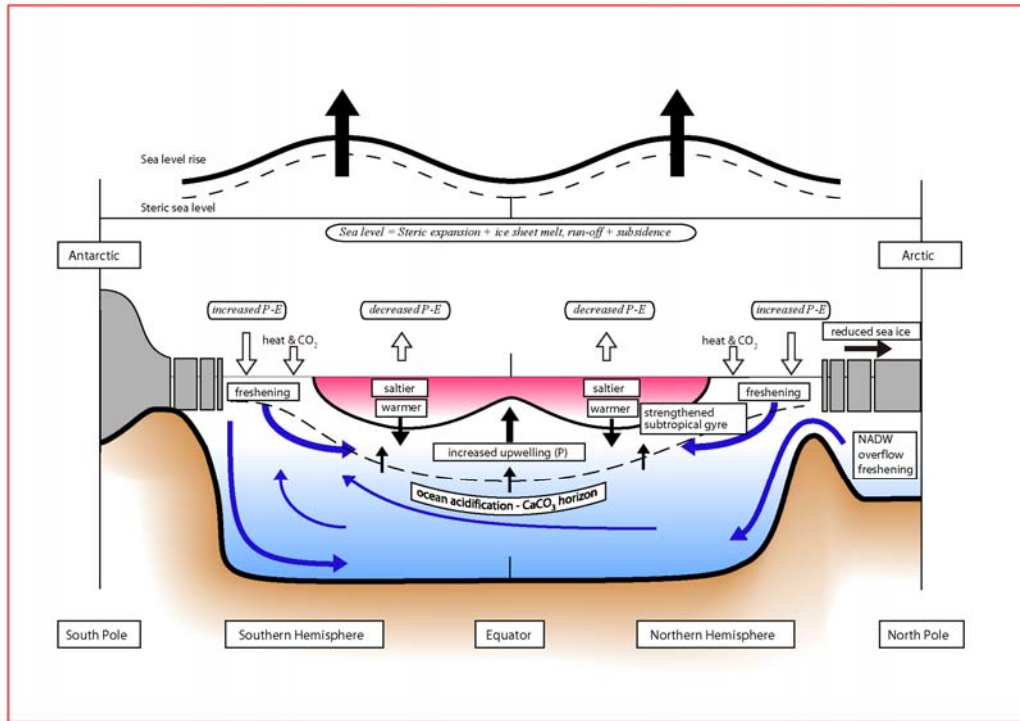
3



4
5
6
7
8
9
10
11

Fig 5.5.10. Estimates for the various contributions to the budget of global-mean sea level change compared with the observed rate of rise for 1993–2003 (upper figure) and the last 4–5 decade (lower figure). The bars shown are ± 2 standard errors. The errors from the separate terms have been combined in quadrature to obtain the error on their total.

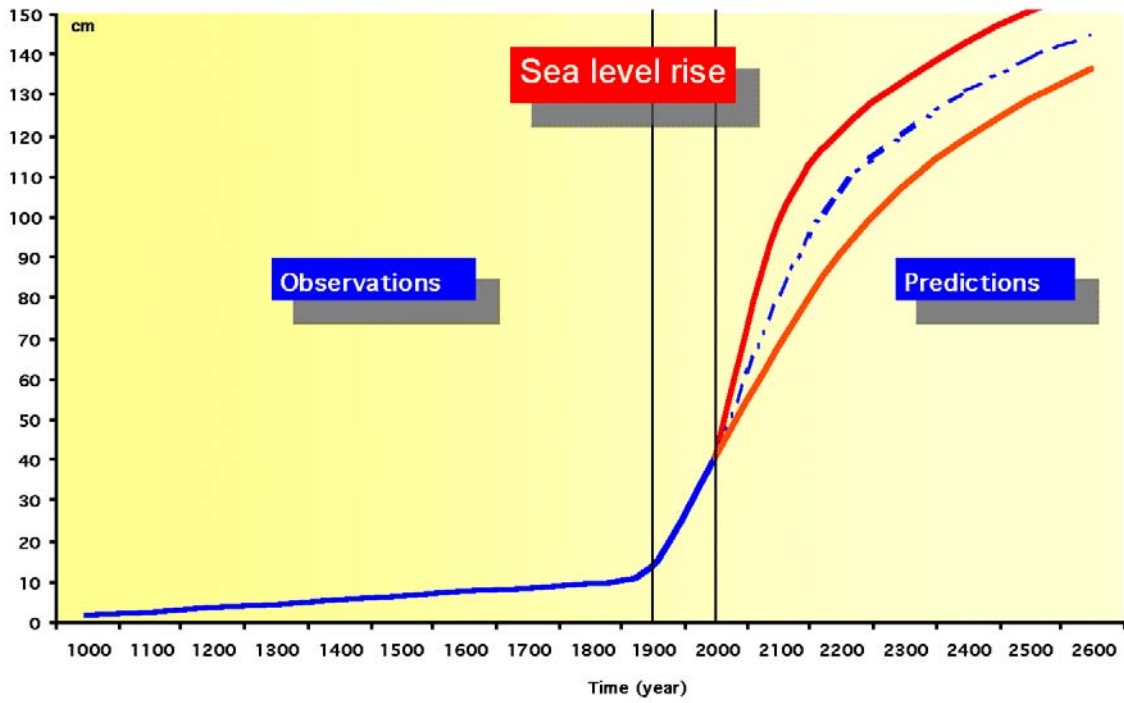
1
2



3
4
5
6
7
8

Figure 5.6.1. Schematic of the observed variations in the ocean state, including ocean temperature, ocean salinity, sea-level, sea-ice and bio-geochemical cycles.

1
2



3
4
5
6
7
8

Question 5.1, Figure 1. Conceptual sketch of the evolution of global sea level in the period 1000–2100. The figure combines the historic reconstructions with instrumental observations with the projections from Chapter 10. The values after 1900 will be replaced in the next draft by quantitative estimates.